GSA Data Repository 2016132

Direct shear fabric dating constrains early Oligocene onset of the South Tibetan detachment in the western Nepal Himalaya

Soucy La Roche et al.

SUPPLEMENTARY METHODS

Quartz crystallographic <c>-axis preferred orientations

Quartz crystallographic <c>-axis preferred orientations (CPO; Law, 1990 and references therein) were measured by Camille Partin with a G50 Automated Fabric Analyzer at the University of Saskatchewan, Saskatoon, Saskatchewan, with a 5 µm resolution on a thin section cut perpendicular to the foliation and parallel to the lineation (Wilson et al., 2007; Peternell et al., 2010; Wilson and Peternell, 2011). This method gives results equivalent to those determined using X-ray (Wilson et al. 2007) and electron back-scattered diffraction (EBSD) (Peternell et al., 2010, 2011). Quartz grains were manually picked with the INVESTIGATOR software (Peternell et al., 2010) and a retardation and geometric quality filter (>80%) was applied to all the optical axes plunging less than 70° to the surface of the thin section. CPO fabrics can be used to quantitatively determine the temperature of deformation ± 50 °C, assuming that strain rate and hydrolytic weakening are not primary controls on the critical resolved shear stress for active slip systems (Kruhl, 1998; Law et al., 2004; Morgan and Law, 2004; Law, 2014). All <c> axis orientation data are presented in equal-area lower-hemisphere stereographic projections oriented such that foliation is represented by a vertical east-west plane and lineation by a horizontal east-west line. Stereographic projections were produced with *Stereonet* (v9) software package of R. Allmendinger.

U-Th/Pb Petrochronology

Monazite were identified in thin section using a mineral liberation analyzer 650 field emission gun environmental scanning electron microscope (MLA 650 FEG ESEM; Fandrich et al., 2007) at Queen's University, Kingston, Ontario, Canada with the help of Agatha Dobosz. Suitable monazite was selected on the basis of size, lack of cracks and inclusions and relationship to deformation fabrics.

Recent studies highlight the need for chemical characterization of monazite to distinguish between different episodes of monazite (re-)crystallization and to avoid sampling multiple domains (Gibson et al., 2004; Kohn et al., 2005; Martin et al., 2007; Cottle et al., 2009; Larson et al., 2011). Selected monazite grains were therefore chemically mapped for U, Th, Y, Ca and Si at Queen's University, Kingston, Ontario, Canada, with wavelength dispersive spectrometry on a JEOL JXA-8230 electron microprobe under the supervision of Brian Joy. The electron microprobe experimental conditions were set at an acceleration voltage of 15 kV, beam current of 200 nA, dwell time of 100 ms and step size of 0.5-0.6 µm. X-ray maps were used to identify zonation, detect inclusions and select laser spot locations.

Three to sixteen 9.7 µm large spots per grain were analyzed in 7 monazite grains for U-Th/Pb isotopes and trace element concentrations by laser-ablation split stream using dual multi-collector-single-collector inductively-coupled plasma mass spectrometry (LASS-ICPMS) at University of California, Santa Barbara, California, United States of America. Analytical methods are described in Cottle et al. (2012, 2013) and Kylander-Clark et al. (2013). Mass bias and Pb/U and Pb/Th downhole fractionation were monitored and corrected for using a primary reference monazite, “44069” (424 Ma, Pb/U isotope dilution-thermal ionization mass spectrometry age (ID-TIMS) (Aleinikoff et al., 2006)). A secondary reference monazite “FC-1” (55.7

Ma Pb/U ID-TIMS age, (Horstwood et al., 2003)) was analyzed concurrently once every eight unknowns to monitor isotopic data accuracy. Trace element concentrations were normalized to an in-house reference "Bananeira" monazite and, based on the long-term reproducibility of secondary reference monazites, are accurate to 3-5%. During the analytical period, repeat analyses of FC-1 gave a weighted mean $^{206}Pb/^{238}U$ date of 56.4 ± 0.2, mean square weighted deviation (MSWD) = 2.0 (n=71), and a weighted mean $^{208}Pb/^{232}Th$ date of 55.8 ± 0.3 Ma, MSWD= 1.9 (n = 60). Data reduction, including corrections for baseline, instrumental drift, mass bias, downhole fractionation, and uncorrected date calculations were carried out using Iolite version 2.5. Full details of the data reduction methodology can be found in Paton et al. (2010). Diagrams were constructed with Excel 2013. All uncertainties are quoted at 2σ and include contributions from the external reproducibility of the primary reference material for the $^{207}Pb/^{206}Pb$, $^{206}Pb/^{238}U$ and $^{208}Pb/^{232}Th$ ratios.

Despite much care in selecting analytical spots, analyses overlapping with more than one chemical domain, with inclusions or with matrix material can occur in grains with narrow chemical domains or because of the depth of the ablation pit (3-4 μm). We identified suspect analyses based on a comparison of ablated monazite grains microphotographs with chemical maps and based on the time-resolved isotopic signal. Such analyses were excluded from geochronological results and interpretations. Mixed domain analyses can nonetheless go undetected if the boundary between the two domains was, at depth, perpendicular to the ablation surface. This would result in ablation of monazite in equal proportions from both domains throughout the ablation pit and would produce a stable, mixed signal of intermediate date and trace element composition.

Himalayan monazite grains, due to their young age, have little accumulated

radiogenic ^{207}Pb and therefore yield imprecise $^{207}Pb/^{235}U$ dates, which in addition, makes a correction for common Pb less accurate and precise. Furthermore, excess ^{206}Pb from unsupported ^{230}Th decay (Schärer, 1984) results in $^{206}Pb/^{238}U$ dates that are too old relative to the 'true' date. Therefore in this study only $^{208}Pb/^{232}Th$ dates, uncorrected for common-lead, are used for interpretations. A common lead correction is not necessary for $^{208}Pb/^{232}Th$ dates, given the high thorigenic component to monazite. This is supported by visual inspection of $^{208}Pb/^{232}Th$ versus $^{206}Pb/^{238}U$ Concordia plots in which analyses with the least 'excess' ^{206}Pb are essentially concordant.

$^{40}Ar/^{39}Ar$ step-heating and total fusion analyses

Samples were gently crushed and sieved, and then rinsed several times with water to remove fine particles. A small amount of the 250-707 μm fraction of crushed material was placed in a Petri dish with ample amounts of ultra-pure ethyl alcohol. The best quality mineral grains or grain aggregates were then picked under a binocular microscope and allowed to dry completely. Individual mineral separates were loaded into 2-3 mm-deep aluminum foil packets which were subsequently stacked vertically into 35-mm long foil tubes and placed into the tubular holes of an aluminum cylinder. Several flux monitor grains of Fish Canyon tuff sanidine (FCT-SAN) (28.201 ± 0.023 1σ Ma; Kuiper et al., 2008) were loaded into each sample packet. J values were interpolated for samples situated between the spaced FCT-SAN monitor grains. GA 1550 biotite (99.15 ± 0.8 1σ Ma, Spell and McDougall (2003) recalculated to FCT-SAN at 28.201 ± 0.023 1σ Ma, and Min et al. (2000) decay constant) was used as a secondary standard to confirm the accuracy of the interpolations. GSC Irradiations #70 and #71 were each shielded with Cd and irradiated for 160 MWH in medium flux position 8B at the research nuclear reactor of McMaster University (MNR) in

Hamilton, Ontario, Canada. Neutron fluence was c. 0.9 x 10^{13} neutrons/cm^2 operating at a 2.5 MW power level. Correction factors for typical interference species produced by thermal neutrons during irradiation are included in the footnote of Table DR2. Samples and monitors were loaded into 1.5 mm diameter pits in a copper planchet and placed under vacuum in an all-metal extraction line. Individual aliquots were step wise heated and analyzed, or fused at high power using a Photon Machines Ltd. Fusion 10.6 55W CO_2 laser coupled to a Nu Instruments Noblesse multicollector mass spectrometer operated at the Geological Survey of Canada, Ottawa, Ontario, Canada. Laser energy was homogenized over a beam radius of 2 mm, gradually increased over 60 s and subsequently held at full power for 30 s. The released gas was then exposed to SAES™ NP-10 (c. 400˚C) and HY-STOR® 201 (room temperature) getters in the extraction line for six minutes. Following gettering, the sample gas was expanded into the mass spectrometer. The Nu Noblesse (model 018) is a single-focusing, Nier-source, 75 magnetic sector multicollector noble gas spectrometer equipped with two quadrupole lens arrays. Ar ions were measured with a fixed array of three ETP® discrete dynode ion-counting multipliers. Data collection followed the measurement scheme MC-Y detailed in Kellett and Joyce (2014). Blanks were run every 4th analysis, in an identical manner to unknowns. Air shots were analyzed every 8th analysis to monitor efficiency and mass fractionation. Full results including blank measurements are included in Table DR2. Sensitivity of the Nu Noblesse at the time of analyses was 7.1-7.5 Amps/mol. Data collection, reduction, error propagation, date calculation and plotting were performed using the software MassSpec (version 7.93) (Deino, 2001), and the $^{40}K/^{40}Ar$ decay constant of Min et al. (2000). Weighted mean calculations and plotting were performed with Isoplot (version 4.15) (Ludwig, 2012). The grains were not conducive to progressive step heating, and degassing occurred at

low power over few heating steps. The attempt to more evenly degas the grains results in several heating steps with very little gas and large associated uncertainties. Thus, only steps comprising >1% ^{39}Ar released are presented on date spectra and inverse isochron diagrams, and used for date calculations. All uncertainties are quoted at 2σ.

INTERPRETATION OF ^{40}AR/^{39}AR RESULTS

Eight total fusion dates on single grains range from 17.6 ± 0.2 Ma to 20.1 ± 0.3 Ma (Fig. DR3A). Differences in diffusion radius, resulting in differences in closure temperatures, cannot account for the 2.5 m.y. date spread. Analyzed muscovite had radii between 125 and 350 µm, a difference that may produce a c. 25 °C variation in closure temperature (Harrison et al., 2009), resulting in date variations of at most 1 m.y. with a relatively slow cooling rate of -25 °C/m.y. (e.g. Imayama et al., 2012). For higher cooling rates (e.g. Sorcar et al., 2014; Wang et al., 2015), date variations due to grain size differences would be even smaller.

The date spectra of four different step heated grains provide insights on the possible causes for older and younger dates. Two aliquots (3409-05 and 3477-07) yield older dates for initial heating steps compared to subsequent steps, suggesting the presence of extraneous ^{40}Ar (Fig. DR3C and E; McDougall and Harrison, 1999). The gas released during these initial steps has a different chemical composition, evidenced by elevated Ca/K and Cl/K (Fig. DR3C and E). This suggest interaction with a fluid that contained dissolved Ca, Cl and Ar, which may have been incorporated in the muscovite as fluid inclusions or could be responsible for back-diffusion of argon into the crystalline structure (Kelley, 2002). The 309 ± 5 ^{40}Ar/^{36}Ar intercept in the inverse isochron of aliquot 3477-07 is slightly above the atmospheric composition ratio of 298.56 (Lee et al. 2006; Mark et al. 2011) and also suggests the presence of a small excess ^{40}Ar component in this aliquot. The inverse isochron date of 18.0 ± 0.2 Ma for

146 this aliquot accounts for excess ^{40}Ar and is equivalent, within uncertainty, with the
147 step heat plateau date (18.1 ± 0.2) that does not account for the excess ^{40}Ar
148 component. The statistically insignificant variation between these two dates suggests
149 that the effect of any excess ^{40}Ar component is within the uncertainty of the step heat
150 dates. Nonetheless, the presence of excess ^{40}Ar likely accounts for older dates in total
151 fusion experiments and some initial steps of the step heating experiments.
152 A third aliquot (3409-04) yields two young initial steps, indicative of ^{40}Ar loss (Fig.
153 DR3B; McDougall and Harrison, 1999). This is further supported by the 261 ± 9
154 $^{40}Ar/^{36}Ar$ intercept in the inverse isochron for this aliquot (Fig. DR3F), below the
155 atmospheric composition ratio of 298.56 (Lee et al. 2006; Mark et al. 2011). Partial
156 recrystallization of muscovite during deformation below its isotopic closure
157 temperature could cause ^{40}Ar loss. In sample JD-46B, grain boundary migration is the
158 dominant quartz recrystallization mechanism, indicating temperature of deformation
159 above 500 °C. Moreover, a CPO fabric from an adjacent quartzite sample indicates a
160 temperature of deformation of 600 ± 50°C. Muscovite occurs in S-, C- and C'-planes,
161 suggesting pre- to syn-kinematic growth. Muscovite is straight and display uniform
162 extinction, although very few grains are bent around garnet porphyroblasts and
163 display undulose extinction. No low-temperature deformation textures such as quartz
164 bulging or subgrain rotation, brittle fractures or kinked mica flakes were observed.
165 These textures all suggest that deformation occurred at a temperature well above the
166 isotopic closure of muscovite (465-480 °C for a 350 μm radius, 50-100 °C/Ma
167 cooling rate at 500 MPa, Harrison et al. 2009), and that the rocks did not experience
168 post-cooling deformation that could have induced ^{40}Ar loss.
169 A second possibility for post-cooling ^{40}Ar loss is the interaction with a fluid that could
170 leach Ar out of the muscovite crystal. Ca/K and Cl/K for the two first young steps of

aliquot 3405-04 are not significantly higher or lower compared to that of subsequent heating steps of the aliquot, implying that fluid did not alter the Ca and Cl content of the grain (Fig. DR3B). Epidote, an unusual mineral for metapelite of typical composition, was observed locally on the outcrop, but no other clear evidence for fluid interaction, such as chloritization or veining, was observed at the outcrop and thin section scales. Even if the cause of the ^{40}Ar loss remains speculative, minor post-cooling ^{40}Ar loss can nonetheless account for the few young dates in the total fusion experiments.

Besides older and younger dates explained by minor excess argon and argon loss, respectively, the sample is dominated by an Ar isotopic composition equating to dates between 19 and 18 Ma, as evidenced by the weighted mean date from the total fusion data (18.7 ± 0.7 Ma), plateau dates of 18.8 ± 0.3 Ma and 18.1 ± 0.2 Ma (aliquot 3409-05 and 3477-07), and two large individual degassing steps at 18.5 ± 0.4 and 18.9 ± 0.1 Ma in aliquot 3477-02, which comprise 25 and 59%, respectively, of the ^{39}Ar released in that grain (Fig. DR3A and C-E). Because aliquot 3409-05 yields a plateau comprising the greatest percentage of released ^{39}Ar (95.5%; Fig. DR3C), and because its inverse isochron date (18.8 ± 0.3 Ma, ^{40}Ar/^{36}Ar intercept of 299 ± 5; Fig. DR3G) is indistinguishable from the plateau date, we interpret this aliquot as the most representative cooling age for the sample.

REFERENCES CITED IN THE SUPPLEMENTARY MATERIAL

Aleinikoff, J.N., Schenck, W.S., Plank, M.O., Srogi, L., Fanning, C.M., Kamo, S.L., and Bosbyshell, H., 2006, Deciphering igneous and metamorphic events in high-grade rocks of the Wilmington Complex, Delaware: Morphology, cathodoluminescence and backscattered electron zoning, and SHRIMP U-Pb geochronology of zircon and monazite: Geological Society of America Bulletin,

v. 118, p. 39-64, doi:10.1130/B25659.1.

Cottle, J.M., Searle, M.P., Horstwood, M.S., and Waters, D.J., 2009, Timing of midcrustal metamorphism, melting, and deformation in the Mount Everest region of southern Tibet revealed by U (-Th)-Pb geochronology: The Journal of Geology, v. 117, p. 643-664, doi:10.1086/605994.

Cottle, J.M., Kylander-Clark, A.R., and Vrijmoed, J.C., 2012, U–Th/Pb geochronology of detrital zircon and monazite by single shot laser ablation inductively coupled plasma mass spectrometry (SS-LA-ICPMS): Chemical Geology, v. 332, p. 136-147, doi:10.1016/j.chemgeo.2012.09.035.

Cottle, J.M., Burrows, A.J., Kylander-Clark, A., Freedman, P.A., and Cohen, R.S., 2013, Enhanced sensitivity in laser ablation multi-collector inductively coupled plasma mass spectrometry: Journal of Analytical Atomic Spectrometry, v. 28, p. 1700-1706, doi:10.1039/c3ja50216c.

Deino, A.L., 2001, User's manual for Mass Spec v. 5.02: Berkeley Geochronology Center Special Publication 1a, 119 p.

Fandrich, R., Gu, Y., Burrows, D., and Moeller, K., 2007, Modern SEM-based mineral liberation analysis: International Journal of Mineral Processing, v. 84, p. 310-320, doi:10.1016/j.minpro.2006.07.018.

Gibson, H.D., Carr, S.D., Brown, R.L., and Hamilton, M.A., 2004, Correlations between chemical and age domains in monazite, and metamorphic reactions involving major pelitic phases: an integration of ID-TIMS and SHRIMP geochronology with Y–Th–U X-ray mapping: Chemical Geology, v. 211, p. 237-260, doi:10.1016/j.chemgeo.2004.06.028.

Ghosh, S.K., and Ramberg, H., 1976, Reorientation of inclusions by combination of pure shear and simple shear: Tectonophysics, v. 34, p. 1-70, doi:10.1016/0040-

1951(76)90176-1.

Horstwood, M.S., Foster, G.L., Parrish, R.R., Noble, S.R., and Nowell, G.M., 2003, Common-Pb corrected in situ U–Pb accessory mineral geochronology by LA-MC-ICP-MS: Journal of Analytical Atomic Spectrometry, v. 18, p. 837-846, doi:10.1039/b304365g.

Imayama, T., Takeshita, T., Yi, K., Cho, D.L., Kitajima, K., Tsutsumi, Y., Kayama, M., Nishido, H., Okumura, T., Yagi, K., and Itaya, T., 2012, Two-stage partial melting and contrasting cooling history within the Higher Himalayan Crystalline Sequence in the far-eastern Nepal Himalaya: Lithos, v. 134, p. 1-22, doi:10.1016/j.lithos.2011.12.004.

Kellett, D.A., and Joyce, N., 2014, Analytical details of single- and multi-collection $^{40}Ar/^{39}Ar$ measurements for conventional step-heating and total fusion age calculation using the Nu Noblesse at the Geological Survey of Canada: analytical details: Geological Survey of Canada, Technical Note 8, 27 p., doi:10.4095/293465.

Kelley, S., 2002, Excess argon in K–Ar and Ar–Ar geochronology: Chemical Geology, v. 188, p. 1-22, doi:10.1016/S0009-2541(02)00064-5.

Kohn, M.J., Wieland, M.S., Parkinson, C.D., and Upreti, B.N., 2005, Five generations of monazite in Langtang gneisses: implications for chronology of the Himalayan metamorphic core: Journal of Metamorphic Geology, v. 23, p. 399-406, doi:10.1111/j.1525-1314.2005.00584.x.

Kruhl, J.H., 1998, Reply: Prism-and basal-plane parallel subgrain boundaries in quartz: A microstructural geothermabarometer: Journal of Metamorphic Petrology, v. 16, p. 142-146, doi:10.1046/j.1525-1314.1996.00413.x.

Kuiper, K.F., Deino, A., Hilgen, F.J., Krijgsman, W., Renne, P.R., and Wijbrans, J.R.,

246 2008, Synchronizing rock clocks of Earth history: Science, v. 320, p. 500-504,
247 doi:10.1126/science.1154339.
248 Kylander-Clark, A.R., Hacker, B.R., and Cottle, J.M., 2013, Laser-ablation split-
249 stream ICP petrochronology: Chemical Geology, v. 345, p. 99-112,
250 doi:10.1016/j.chemgeo.2013.02.019.
251 Larson, K.P., Cottle, J.M., and Godin, L., 2011, Petrochronologic record of
252 metamorphism and melting in the upper Greater Himalayan sequence, Manaslu–
253 Himal Chuli Himalaya, west-central Nepal: Lithosphere, v. 3, p. 379-392,
254 doi:10.1130/L149.1.
255 Law, R.D., 1990, Crystallographic fabrics: a selective review of their applications to
256 research in structural geology: Geological Society, London, Special Publications,
257 v. 54, p. 335-352, doi:10.1144/GSL.SP.1990.054.01.30.
258 Law, R.D., 2014, Deformation thermometry based on quartz c-axis fabrics and
259 recrystallization microstructures: a review: Journal of Structural Geology, v. 66,
260 p. 129-161, doi:10.1016/j.jsg.2014.05.023.
261 Law, R.D., Searle, M.P., and Simpson, R.L., 2004, Strain, deformation temperatures
262 and vorticity of flow at the top of the Greater Himalayan Slab, Everest Massif,
263 Tibet: Journal of the Geological Society, v. 161, p. 305-320, doi:10.1144/0016-
264 764903-047.
265 Lee, J.Y., Marti, K., Severinghaus, J.P., Kawamura, K., Yoo, H.S., Lee, J.B., and Kim,
266 J.S., 2006, A redetermination of the isotopic abundances of atmospheric Ar:
267 Geochimica et Cosmochimica Acta, v. 70, p. 4507-4512,
268 doi:10.1016/j.gca.2006.06.1563.
269 Ludwig, K., 2012, User's manual for Isoplot version 3.75-4.15: a geochronological
270 toolkit for Microsoft Excel: Berkley Geochronological Center Special

Publication, (5).

Mark, D.F., Stuart, F.M., and De Podesta, M., 2011, New high-precision measurements of the isotopic composition of atmospheric argon: Geochimica et Cosmochimica Acta, v. 75, p. 7494-7501, doi:10.1016/j.gca.2011.09.042.

Martin, A.J., Gehrels, G.E., and DeCelles, P.G., 2007, The tectonic significance of (U, Th)/Pb ages of monazite inclusions in garnet from the Himalaya of central Nepal: Chemical Geology, v. 244, 1-24, doi:10.1016/j.chemgeo.2007.05.003.

McDougall, I., and Harrison, T.M., 1999, Geochronology and Thermochronology by the $^{40}Ar/^{39}Ar$ Method: Oxford University Press.

Min, K., Mundil, R., Renne, P.R., and Ludwig, K.R., 2000, A test for systematic errors in $^{40}Ar/^{39}Ar$ geochronology through comparison with U-Pb analysis of a 1.1 Ga rhyolite: Geochimica et Cosmochimica Acta, v. 64, p. 73-98, doi:10.1016/S0016-7037(99)00204-5.

Morgan, S.S., and Law, R.D., 2004, Unusual transition in quartzite dislocation creep regimes and crystal slip systems in the aureole of the Eureka Valley–Joshua Flat–Beer Creek pluton, California: a case for anhydrous conditions created by decarbonation reactions: Tectonophysics, v. 384, p. 209-231, doi:10.1016/j.tecto.2004.03.016.

Paton, C., Woodhead, J.D., Hellstrom, J.C., Hergt, J.M., Greig, A., and Maas, R., 2010, Improved laser ablation U-Pb zircon geochronology through robust downhole fractionation correction: Geochemistry, Geophysics, Geosystems, v. 11, p. 1-36, doi:10.1029/2009GC002618.

Peternell, M., Hasalová, P., Wilson, C.J., Piazolo, S., and Schulmann, K., 2010, Evaluating quartz crystallographic preferred orientations and the role of deformation partitioning using EBSD and fabric analyser techniques: Journal of

296 Structural Geology, v. 32, p. 803-817, doi:10.1016/j.jsg.2010.05.007.
297 Peternell, M., Russell-Head, D.S., and Wilson, C.J.L., 2011, A technique for recording
298 polycrystalline structure and orientation during in situ deformation cycles of rock
299 analogues using an automated fabric analyser: Journal of microscopy, v. 242, p.
300 181-188, doi:10.1111/j.1365-2818.2010.03456.x.
301 Schärer, U., 1984, The effect of initial ^{230}Th disequilibrium on young U-Pb ages: the
302 Makalu case, Himalaya: Earth and Planetary Science Letters, v. 67, p. 191-204,
303 doi:10.1016/0012-821X(84)90114-6.
304 Spell, T.L., and McDougall, I., 2003, Characterization and calibration of ^{40}Ar/^{39}Ar
305 dating standards: Chemical Geology, v. 198, p. 189-211, doi:10.1016/S0009-
306 2541(03)00005-6.
307 Sorcar, N., Hoppe, U., Dasgupta, S., and Chakraborty, S., 2014, High-temperature
308 cooling histories of migmatites from the High Himalayan Crystallines in Sikkim,
309 India: rapid cooling unrelated to exhumation?: Contributions to Mineralogy and
310 Petrology, v. 167, p. 1-34, doi:10.1007/s00410-013-0957-3.
311 Wang, J.M., Rubatto, D., and Zhang, J.J., 2015, Timing of Partial Melting and
312 Cooling across the Greater Himalayan Crystalline Complex (Nyalam, Central
313 Himalaya): In-sequence Thrusting and its Implications: Journal of Petrology, v.
314 56, p. 1677-1702, doi:10.1093/petrology/egv050.
315 Wilson, C.J.L., Russell-Head, D.S., Kunze, K., and Viola, G., 2007, The analysis of
316 quartz c-axis fabrics using a modified optical microscope: Journal of
317 microscopy, v. 227, p. 30-41, doi:10.1111/j.1365-2818.2007.01784.x
318 Wilson, C.J., and Peternell, M., 2011, Evaluating ice fabrics using fabric analyser
319 techniques in Sørsdal Glacier, East Antarctica: Journal of Glaciology, v. 57, p.
320 881-894, doi:10.3189/002214311798043744.

SUPPLEMENTARY TABLES

Data Table DR1. Monazite U-Th/Pb geochronology

Data Table DR2. Muscovite $^{40}Ar/^{39}Ar$ thermochronology

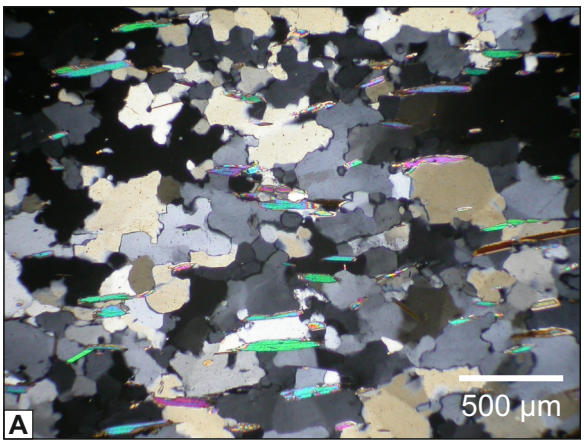

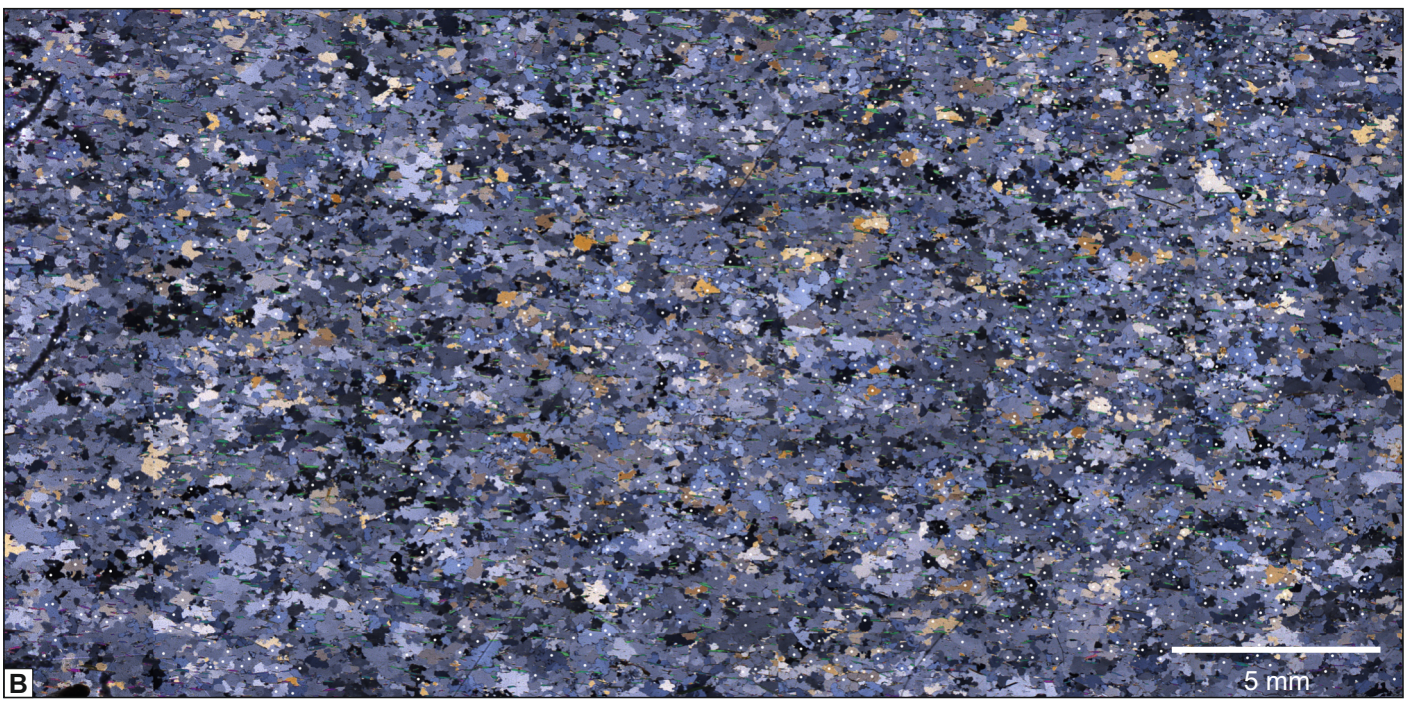

Fig. DR1. A. Cross-polarized light photomicrograph of grain boundary migration microstructure in quartzite JD-46A. B. Lambda-0 photomicrograph of quartzite JD-46A with the location of each quartz crystallographic <c>-axis orientations indicated by a white dot.

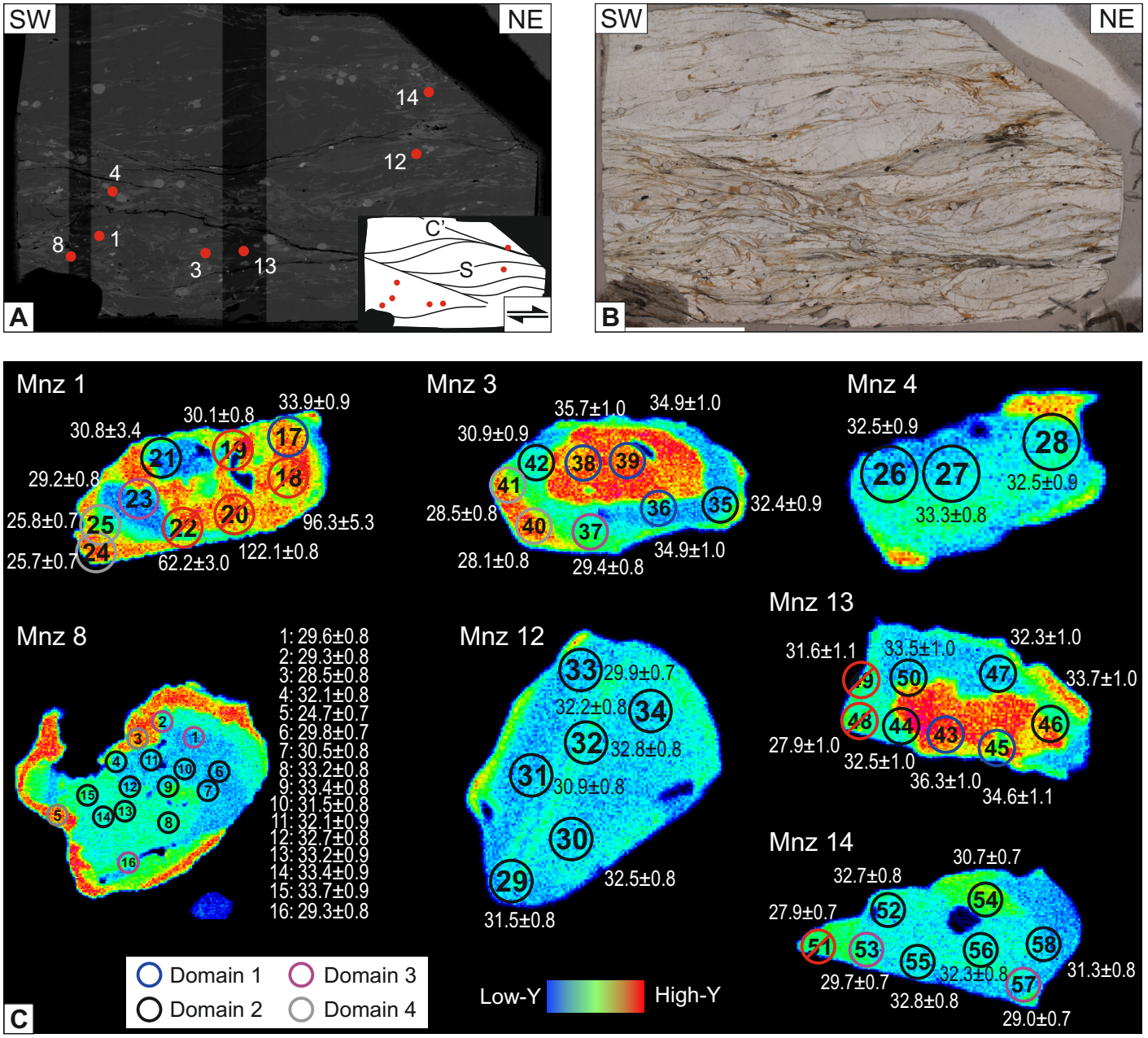

Fig. DR2. A: Back-scattered electron image of thin section JD-46B with location of analyzed monazite grains. Foliation (S) and top-to-the-NE shear bands (C') are outlined in the inset. B: Thin section photograph in plane polarized light of thin section JD-46B. C: Maps of relative Y concentration of all analyzed monazite grains with date spots in Ma. Numbers inside each circle refer to analysis number. Each spot is 9.7 µm large and color coded according to domain attribution. Note that trace element contents used for analysis classification were acquired with LASS-ICPMS. Hence, the relative Y concentration map may be misleading if a significant portion of the ablated material belonged to a domain underlying the surficial domain observed in the map. These analyses were used for interpretation only if a significant portion of the isotopic signal was stable enough to calculate a reliable date and trace element composition. Red date spots were discarded for age interpretations because they overlap with matrix material, inclusions, or more than one chemical domain. Note that Group 4 analyses were obtained in the two shortening quadrants of only one monazite grain (#8) because the low aspect ratio (c. 1:1) of that specific grain would allow infinite rotation under general shear strain instead of resting in the flow plane (Ghosh and Ramberg, 1976). D: Plane-polarized light photomicrograph of garnet wrapped by the foliation and containing randomly oriented quartz inclusions, attesting for pre-kinematic growth. Resorbed margins are likely the consequence of decompression. Bt—biotite; Grt—garnet; Ms—muscovite; Qtz—quartz; rm—resorbed margins.

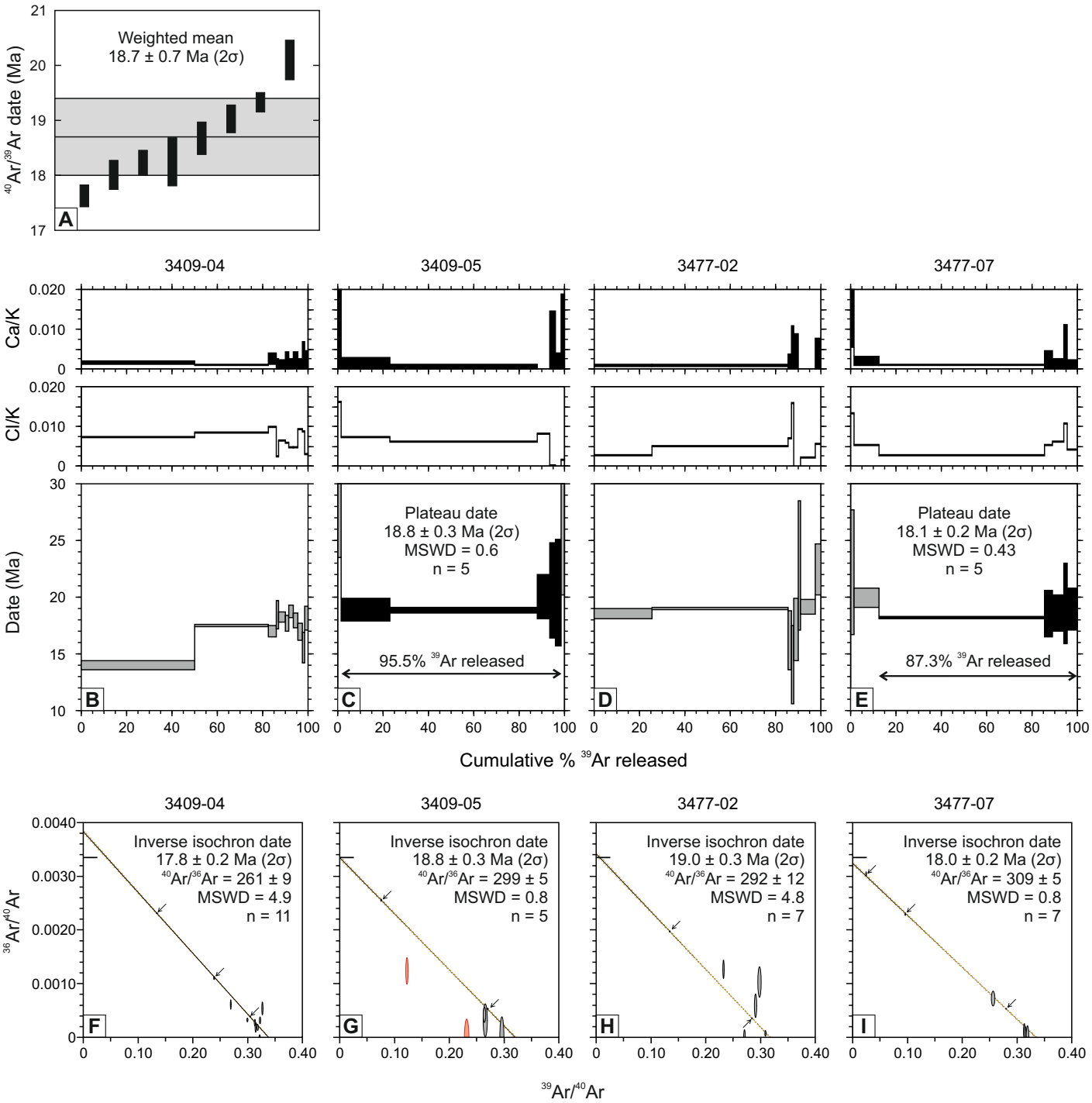

Fig. DR3. Muscovite $^{40}Ar/^{39}Ar$ dates of sample JD-46B. A: Weighted average plot of all total fusion dates. B-E: step-heating date spectra with Ca/K and Cl/K of each individual steps. F-I: Inverse isochron plots. Data ellipses in red on the inverse isochron plots were not included in the regressions and date calculations because they do not appear to comprise the same population and each yield less than 2% of the released ^{39}Ar. Arrows indicate small data ellipses. All uncertainties are 2σ except the error envelope on the inverse isochron regression lines (1σ). MSWD—mean squared weighted deviation; n—number of analyses in date calculations.